

Enhancing Image Layout Control with Loss-Guided Diffusion Models

Zakaria Patel* Kirill Serkh†

May 24, 2024

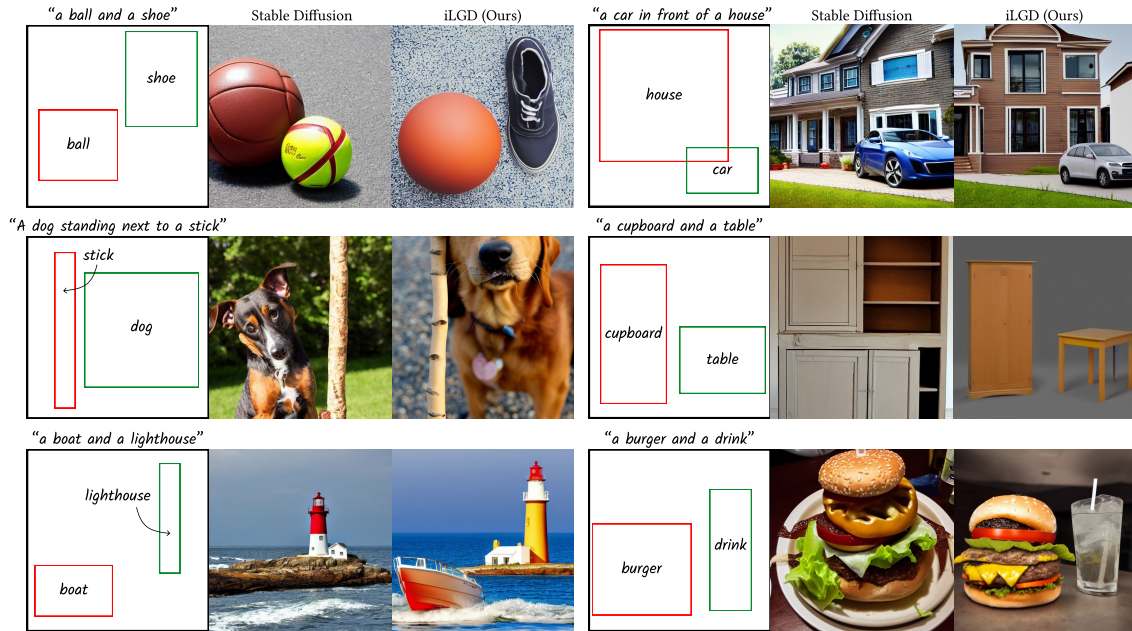


Figure 1: Injection loss guidance (iLGD) uses attention injection and loss guidance to generate high quality images conforming to a given layout. The first column of each set of images depicts the bounding box input to the diffusion model. The second column is the output of Stable Diffusion alone. The third column is our method, using the same random seeds.

Abstract

Diffusion models are a powerful class of generative models capable of producing high-quality images from pure noise. In particular, conditional diffusion models allow one to specify the contents of the desired image using a simple text prompt. Conditioning on a text prompt alone, however, does not allow for fine-grained control over the composition and layout of the final image, which instead depends closely on the initial noise distribution. While most methods which introduce spatial constraints (e.g., bounding boxes) require fine-tuning, a smaller and more recent subset of these methods are training-free. They are applicable whenever the prompt influences the model through an attention mechanism, and generally fall into one of two categories. The first entails modifying the cross-attention maps of specific tokens directly to enhance the signal in certain regions of the image. The second works by defining a loss function over the cross-attention maps, and using the gradient of this loss to guide the latent. While previous work explores these as alternative strategies, we provide an interpretation for these methods which highlights their complimentary features, and demonstrate that it is possible to obtain superior performance when both methods are used in concert.

*Ecoment & Department of Computer Science, University of Toronto
Corresponding author. Email: zakaria.patel@mail.utoronto.ca

†Departments of Mathematics and Computer Science, University of Toronto
Email: kserkh@math.toronto.edu

1 Introduction

Recently, diffusion models (Sohl-Dickstein et al., 2015; Ho et al., 2020; Song and Ermon, 2019) have emerged as a powerful class of generative models capable of producing high quality samples with superior mode coverage. These models are trained to approximate a data distribution, and sampling from this learned distribution can subsequently generate very realistic and diverse images. Incorporating conditioning (Saharia et al., 2022; Ramesh et al., 2022; Rombach et al., 2022) further extends the utility of diffusion models by allowing one to specify the contents of the desired image using a simple text prompt, leveraging the models’ impressive compositional capabilities to combine concepts in ways that may not have been present in the training set. Conditioning on a text prompt does not, however, allow one fine-grained control over the layout of the final image, which is instead highly dependent on the initial noise sample.

An especially simple and intuitive way of describing a layout is to provide bounding boxes for various tokens in the text prompt. One way to realize a model taking such an input is to resort to training-based methods, wherein a pretrained model undergoes additional finetuning using training data where the images have been supplemented by their layouts. While such methods can achieve impressive performance (Zheng et al., 2023; Zhang et al., 2023), this often involves the introduction of additional model complexity and training cost, in addition to the difficult task of compiling the training data. A recently proposed alternative approach (Xie et al., 2023; Chen et al., 2024) uses the cross-attention module to achieve training-free layout control. By defining a loss over the attention maps, and by guiding or iteratively refining the latents to minimize this loss, it is possible to generate images that are reasonably faithful to the desired layout. One drawback, however, is that the ad-hoc choice of a loss function means that the image may be sampled from a low probability region of the learned distribution, particularly if the amount of guidance is high, as it competes with the denoising process described by the model’s learned score function. In this case, the sample suffers from poor image quality, even if the desired layout is achieved. It is also possible to directly modify the attention maps during the denoising process, to create images with high attention in the desired regions (Balaji et al., 2023). This approach, like loss guidance, can also suffer from degraded image quality when the attention modification is sufficiently strong (Chen et al., 2024).

In this paper, we propose injection loss guidance (iLGD), a framework in which the model’s denoising process maintains better agreement with loss guidance, such that sampled images simultaneously present the appropriate layout and maintain good image quality. First, we bias the latent towards the desired layout by altering the model’s attention maps directly, a process which we refer to as attention injection. The goal of injection is not to produce a latent which perfectly adheres to the desired layout, but rather, to produce a latent which is close enough to the desired layout that we can afford to use a smaller amount of loss guidance. In doing so, we reimagine the role of injection as a coarse biasing of the diffusion process, and loss guidance as a refiner. We show that such a framework is capable of controlling the image layout, while achieving superior image quality in many cases.

2 Related Work

2.1 Generative Models

Generative models learn to estimate a data distribution with the goal of generating samples from this distribution. Autoregressive models (Oord et al., 2016; Van Den Oord et al., 2016;

Salimans et al., 2017; Germain et al., 2015) are likelihood-based models that predict a distribution over each pixel in an ordered sequence, given some window of previous pixels. While they are capable of modelling complex dependencies between different variables, they can be computationally expensive to train and inefficient to sample from, particularly when dealing with longer sequences. Generative adversarial networks (GANs) (Goodfellow et al., 2014) are another type of generative model that are based on adversarial training, and are capable of producing high quality samples. However, they are often prone to mode collapse and are sometimes difficult to train. Variational Autoencoders (VAEs) (Kingma and Welling, 2014) are easier to train, but are known to produce blurry samples. Flow models (Rezende and Mohamed, 2015) similarly suffer from lower quality samples, although, like GANs and VAEs, they are efficient to sample from.

More recently, a new family of generative models, known as diffusion models (Sohl-Dickstein et al., 2015; Ho et al., 2020; Song and Ermon, 2019), have achieved superior results on image synthesis compared to the previous state of the art (Dhariwal and Nichol, 2021), with samples exhibiting incredible diversity and image quality. While early diffusion models were formulated as Markov chains and relied on a large number of transitions to generate samples, Song et al. (2021) showed that such a sampling procedure can be viewed as a discretization of a certain stochastic differential equation (SDE). In particular, Song et al. (2021) showed that there exists a family of SDEs, whose solutions are sampling trajectories from the diffusion model. One such SDE, called the probability flow ODE, is completely deterministic and contains no noise. This enables the use of various ordinary differential equation (ODE) solvers for efficient sampling (Karras et al., 2022; Lu et al., 2022).

2.2 Controllable Generation

Diffusion models can use a wide range of techniques for controllable generation. SDEdit (Meng et al., 2022) allows the user to specify a layout by using paint strokes, which are noised to time $t < T$ to provide an initialization for solving the reverse-time SDE. The realism of the final image is, however, sensitive to the initial noise level σ_t , and guiding the generation of new images requires all high-level features to be specified in the stroke image. A more user-friendly method by Voynov et al. (2023) requires only a simple sketch to guide the denoising process. The user-provided sketch is compared with the edges extracted by a latent edge predictor in order to compute a loss, which is used to iteratively refine the latent. In this case, the latent edge predictor must be trained, and sketches of more complicated scenes may be tedious. Zhang et al. (2023) propose a more general method in which a separate encoder network takes as input a conditioning control image, such as a sketch, depth map, or scribble, to guide the generation process. Unfortunately, this requires finetuning a large pretrained encoder. When the inputs are specified as bounding boxes, smaller trainable modules can be used between the layers of the denoising UNet to encode layout information (Zheng et al., 2023). Cheng et al. (2023) also use an additional module which takes in bounding box inputs, injecting it directly after the self-attention layers. Once again, however, neither method can be adapted immediately, as the additional parameters necessitate further training.

A number of other methods have been proposed that are training-free. Bansal et al. (2024) define a generic loss on the noiseless latent $\hat{\mathbf{z}}_0$ predicted from \mathbf{z}_t by Tweedie’s formula, and subsequently perform loss guidance on the latent \mathbf{z}_t at each time step. One downside of this method is that, while the loss expects clean images, the predicted latent $\hat{\mathbf{z}}_0$ is an approximation to only an average of possible generated images, and so can be blurry for large times t . An

alternative approach was proposed by Bar-Tal et al. (2023), who used separate score functions on various regions in a latent diffusion model, with an optimization step at each iteration designed to fuse the separate diffusion paths. While this method can be effective in many cases, it can nonetheless exhibit patchwork artifacts, where the final image appears to be composed of several images rather than depicting a single scene.

Alternatively, several works have explored the use of cross-attention to achieve training-free layout control. Hertz et al. (2023) demonstrate how attention maps can be injected from one diffusion process to another, and reweighted to control the influence of specific tokens. Subsequent work by Balaji et al. (2023) builds upon this idea by directly manipulating the values in the attention map to obtain the desired layout, although it is difficult to precisely localize objects appearing in an image with this method alone. Singh et al. (2023) also use this technique to improve semantic control in stroke-guided image synthesis, which they combine with loss guidance based on the stroke image to improve the realism of generated images. Instead of using strokes, Chen et al. (2024) show that controlling layout with bounding boxes is possible by using loss guidance, where the loss is defined on the attention maps, although this method requires searching for a suitable noise initialization. Concurrent work by Xie et al. (2023) and Couairon et al. (2023) also use attention-based loss guidance; the former adds spatial constraints to control the scale of the generated content, while the latter uses segmentation maps instead of bounding boxes. Epstein et al. (2023) show that it is even possible to control properties of objects in an image, such as their shape, size, and appearance, through their attention maps, and subsequently manipulate these properties through loss guidance.

These works demonstrate the utility of injection, loss guidance, and the general role of cross-attention in layout control. We take a joint approach where we use cross-attention injection to assist loss guidance in producing the desired layout from simple bounding box inputs. In analyzing the role of each technique in layout control, we offer justification for their complementary use. The result is a powerful and intuitive method for layout control which maintains the quality of the generated images.

3 Preliminaries

3.1 Diffusion Models

Diffusion models (Ho et al., 2020) are characterized by two principle algorithms. The first is the forward process, wherein the data \mathbf{x}_0 is gradually corrupted by Gaussian noise until it becomes pure noise, which we denote by \mathbf{x}_T . The reverse process moves in the opposite direction, attempting to recover the data by iteratively removing noise. The denoiser $\epsilon_\theta(\mathbf{x}_t, t)$ is typically a UNet (Ronneberger et al., 2015) which accepts an image \mathbf{x}_t , and predicts its normalized noise content ϵ . Removing a fraction of this noise yields a slightly denoised image \mathbf{x}_{t-1} . Repeating this process over T steps produces a noise-free image \mathbf{x}_0 .

Operating directly on the image \mathbf{x}_t in pixel-space is computationally expensive. As an alternative, latent diffusion models have been proposed to curtail this high cost, in which the denoising procedure is performed in latent space, whose dimensionality is typically much lower than pixel space. Stable Diffusion (Rombach et al., 2022) is one example of a latent diffusion model which achieves state-of-the-art performance on various image synthesis tasks. It leverages a powerful autoencoder to project to and from latent space, where the standard denoising procedure is performed. Images in latent space are typically denoted by \mathbf{z}_t , and the encoder and decoder are denoted by \mathcal{E} and \mathcal{D} , respectively, so that $\mathbf{z}_t = \mathcal{E}(\mathbf{x}_t)$ and $\mathbf{x}_t = \mathcal{D}(\mathbf{z}_t)$.

During training, samples from the true data distribution $q(\mathbf{x}_0)$ are corrupted via the forward process. By training a diffusion model to learn a reverse process in which it iteratively reconstructs these noisy samples into noise-free samples, it is possible to generate images from pure noise at inference time. This corresponds to sampling from an approximation $p_\theta(\mathbf{x}_0)$ to the data distribution, $q(\mathbf{x}_0)$. This generation process can be guided by introducing an additional input vector \mathbf{y} , which is often a text prompt. In this case, the model produces samples from an approximation $p_\theta(\mathbf{x}_0|\mathbf{y})$ to the conditional distribution $q(\mathbf{x}_0|\mathbf{y})$. A more detailed discussion of diffusion models is provided in Appendix A.

3.2 Cross-Attention

To perform conditional image synthesis with text, Stable Diffusion leverages a cross-attention mechanism (Vaswani et al., 2017). Cross-attention enables the modelling of complex dependencies between two sequences $\mathbf{X}^T = (\mathbf{x}_1, \mathbf{x}_2, \dots, \mathbf{x}_n)$ and $\mathbf{Y}^T = (\mathbf{y}_1, \mathbf{y}_2, \dots, \mathbf{y}_k)$, whose elements are projected to query, key and value vectors using projection matrices

$$\mathbf{X}\mathbf{W}_q = \mathbf{Q} \in \mathbb{R}^{n \times d_k}, \quad (1)$$

$$\mathbf{Y}\mathbf{W}_k = \mathbf{K} \in \mathbb{R}^{k \times d_k}, \quad (2)$$

$$\mathbf{Y}\mathbf{W}_v = \mathbf{V} \in \mathbb{R}^{k \times d_v}. \quad (3)$$

Subsequently, the attention weights are computed as

$$A = \text{Softmax} \left(\frac{\mathbf{Q}\mathbf{K}^T}{\sqrt{d_k}} \right) \in \mathbb{R}^{n \times k}. \quad (4)$$

The new representation for the sequence \mathbf{X} is

$$\mathbf{Z} = \mathbf{A}\mathbf{V} \in \mathbb{R}^{n \times d_v}. \quad (5)$$

In diffusion models, the sequence \mathbf{X} represents the image, where each \mathbf{x}_i represents a pixel, and \mathbf{Y} is a sequence of token embeddings. The attention weights A , also called the attention or cross-attention map, follow the same spatial arrangement as the image, and a unique map A_j is produced for each token \mathbf{y}_j in \mathbf{Y} . Each entry A_{ij} describes how strongly related a spatial location \mathbf{x}_i is to the token \mathbf{y}_j . We leverage this feature of cross-attention to guide the image generation process.

3.3 Score Matching

The forward and reverse processes can be modelled by solutions of stochastic differential equations (SDEs) (Song et al., 2021). While determining the coefficients of the forward process SDE is straightforward, the reverse process corresponds to a solution of the reverse-time SDE, which requires learning the score of the intractable marginal distribution $q(\mathbf{x}_t)$. Instead, Song et al. (2021) use the score-matching objective

$$\mathbb{E}_t[\lambda(t)\mathbb{E}_{q(\mathbf{x}_0)}\mathbb{E}_{q(\mathbf{x}_t|\mathbf{x}_0)}[\|\mathbf{s}_\theta(\mathbf{x}_t, t) - \nabla_{\mathbf{x}_t} \log q(\mathbf{x}_t|\mathbf{x}_0)\|_2^2]], \quad (6)$$

for some nonnegative function $\lambda: [0, T] \rightarrow \mathbb{R}$.

While Eq. (6) does not directly enforce learning the score of $q(\mathbf{x}_t)$, it is nonetheless minimized when $\mathbf{s}_\theta(\mathbf{x}_t, t) = \nabla_{\mathbf{x}_t} \log q(\mathbf{x}_t)$ (Vincent, 2011). Conditioning on \mathbf{x}_0 provides a tractable

way to obtain a neural network $\mathbf{s}_\theta(\mathbf{x}_t, t)$ which, given enough parameters, matches $\nabla_{\mathbf{x}_t} \log q(\mathbf{x}_t)$ almost everywhere. Because the forward process $q(\mathbf{x}_t|\mathbf{x}_0)$ is available in closed form, it can be shown that the neural network which minimizes this loss is

$$\mathbf{s}_\theta(\mathbf{x}_t, t) = -\frac{\boldsymbol{\epsilon}_\theta(\mathbf{x}_t, t)}{\sigma_t}, \quad (7)$$

where σ_t is the standard deviation of the forward process at time t , and $\boldsymbol{\epsilon}_\theta(\mathbf{x}_t, t)$ predicts the normalized noise $\boldsymbol{\epsilon} \sim \mathcal{N}(\mathbf{0}, \mathbf{I})$ in \mathbf{x}_t .

When the predicted score function is available, any one of a family of reverse-time SDEs, all with the same marginal distributions $p_\theta(\mathbf{x}_t) \approx q(\mathbf{x}_t)$, can be solved to sample from $p_\theta(\mathbf{x}_0) \approx q(\mathbf{x}_0)$. One of these SDEs is noise-free, and is known as the probability flow ODE. A highly efficient way to sample from $p_\theta(\mathbf{x}_0)$ is to solve the probability flow ODE using a small number of large timesteps (Song et al., 2021). An important benefit of sampling using an ODE is that the sampling process is deterministic, in the sense that it associates each noisy image \mathbf{x}_T with a unique noise-free sample \mathbf{x}_0 (Song et al., 2021).

3.4 Classifier-Free Guidance

In order to generate images following a user-supplied text prompt, the denoiser $\boldsymbol{\epsilon}_\theta(\mathbf{z}_t, t, \mathbf{y})$ of a latent diffusion model is trained with an additional input given by a sequence of token embeddings $\mathbf{y} = \{\mathbf{y}_1, \mathbf{y}_2, \dots, \mathbf{y}_k\}$. A single denoiser, usually a UNet, is trained over a variety of text prompts, and the token embeddings influence the denoiser by a cross-attention mechanism in both the contractive and expansive layers. Ho and Salimans (2021) found that, rather than sampling images using the conditional denoiser alone, better results can be obtained by taking a combination of conditional and unconditional noise estimates,

$$\tilde{\boldsymbol{\epsilon}}_\theta(\mathbf{z}_t, t, \mathbf{y}) = (1 + w)\boldsymbol{\epsilon}_\theta(\mathbf{z}_t, t, \mathbf{y}) - w\boldsymbol{\epsilon}_\theta(\mathbf{z}_t, t, \{\}), \quad (8)$$

where w represents the intensity of the additive term $\boldsymbol{\epsilon}_\theta(\mathbf{z}_t, t, \mathbf{y}) - \boldsymbol{\epsilon}_\theta(\mathbf{z}_t, t, \{\})$. For $-1 \leq w \leq 0$, this noise prediction can be viewed as an approximation to $(-\sigma_t$ times) the score function of the marginal distribution $\tilde{p}_\theta(\mathbf{z}_t|\mathbf{y}) \propto p_\theta(\mathbf{z}_t|\mathbf{y})^{1+w}p_\theta(\mathbf{z}_t|\{\})^{-w}$. In classifier-free guidance (CFG), $w \gg 0$, which does not have a simple interpretation in terms of the marginal distributions of the new denoising process.

In this paper, we denote the CFG noise prediction by $\boldsymbol{\epsilon}_\theta(\mathbf{z}_t, t, \mathbf{y})$, or sometimes just $\boldsymbol{\epsilon}_\theta(\mathbf{z}_t, t)$, when the dependence on \mathbf{y} is clear.

3.5 Controllable Layout Generation

We use BoxDiff (Xie et al., 2023) as our primary point of comparison. In their paper, the authors apply spatial constraints on the attention maps of a latent diffusion model to derive a loss, and directly update the latent at time step t by replacing it with

$$\mathbf{z}'_t = \mathbf{z}_t - \alpha_t \cdot \nabla_{\mathbf{z}_t} \mathcal{L}. \quad (9)$$

The parameter α_t decays linearly with t , and controls the strength of the loss guidance in each iteration. The loss \mathcal{L} is computed as the sum of three separate losses, $\mathcal{L} = \mathcal{L}_{\text{IB}} + \mathcal{L}_{\text{OB}} + \mathcal{L}_{\text{CC}}$, where \mathcal{L}_{IB} encourages the attentions of the target tokens to be large inside the bounding boxes, \mathcal{L}_{OB} penalizes attentions appearing outside of the bounding boxes, and \mathcal{L}_{CC} encourages higher attentions near the corners of the bounding boxes.



Figure 2: The effects of varying the strengths of BoxDiff and attention injection by tuning their respective parameters. In the top row, we sweep through various choices of α_T to tune the guidance strength of BoxDiff. In the bottom row, we sweep through various choices of the injection strength ν' . For iLGD, shown in the final column, we use $\nu' = 0.75$ and $\eta = 0.8$.

4 Method

4.1 Attention Injection

Hertz et al. (2023) observed that, by extracting the attention maps from a latent diffusion process and applying them to another one with a modified token sequence, it is possible to transfer the composition of an image. This technique is very effective, but requires an original set of attention maps which produce the desired layout, and it is not feasible to generate images until this layout is obtained.

Instead, we rely on the observation that the attention maps early in the diffusion process are strong indicators of the generated image’s composition. For early timesteps, both the latents and the attention maps are relatively diffuse, and don’t suggest any fine details about objects in the image. Motivated by this, we manipulate the attention maps by artificially enhancing the signal in certain regions. Given a list of target tokens $S \subset \{1, 2, \dots, k\}$, we define $m = \{\mathbf{m}_1, \mathbf{m}_2, \dots, \mathbf{m}_k\} \in \mathbb{R}^{n \times k}$ by setting each mask \mathbf{m}_j , $j \in S$, equal to 1 over the region that the text token \mathbf{y}_j should correspond to, and zero otherwise, and perform injection by replacing the cross-attention map A_t at time t with

$$A'_t = \text{softmax} \left(\frac{\mathbf{Q}_t \mathbf{K}_t^T + \nu_t m}{\sqrt{d_k}} \right), \quad (10)$$

for some $\nu_t > 0$. We follow Balaji et al. (2023) and use the scaling

$$\nu_t = \nu' \cdot \log(1 + \sigma_t) \cdot \max(\mathbf{Q}_t \mathbf{K}_t^T). \quad (11)$$

Scaling by σ_t ensures the injection strength is appropriate for a given timestep, and ν' is a constant which controls the overall strength of injection.

This way, we directly bias the model’s predicted score $\mathbf{s}_\theta(\mathbf{x}_t, t) \approx \nabla_{\mathbf{z}_t} \log q_t(\mathbf{z}_t | \mathbf{y})$ so that each latent \mathbf{z}_{t-1} more closely corresponds to the desired layout. We denote the corresponding modified noise prediction by $\epsilon_\theta(\mathbf{z}_t, t, A_t \xrightarrow{\nu', m} A'_t)$.

4.2 Loss Guidance

Conditional latent diffusion models predict the time-dependent conditional score $\nabla_{\mathbf{z}_t} \log q(\mathbf{z}_t|\mathbf{y})$, so that the resulting latent at the end of the denoising process is sampled from $q(\mathbf{z}_0|\mathbf{y})$. We can modify the conditional score at time t by introducing a loss term $\ell_{\mathbf{y}}(\mathbf{z}_t)$,

$$\nabla_{\mathbf{z}_t} \log \hat{q}(\mathbf{z}_t|\mathbf{y}) = \nabla_{\mathbf{z}_t} \log q(\mathbf{z}_t|\mathbf{y}) - \eta \nabla_{\mathbf{z}_t} \ell_{\mathbf{y}}(\mathbf{z}_t), \quad (12)$$

which corresponds to the marginal distribution

$$\hat{q}(\mathbf{z}_t|\mathbf{y}) \propto q(\mathbf{z}_t|\mathbf{y}) e^{-\eta \ell_{\mathbf{y}}(\mathbf{z}_t)}. \quad (13)$$

The scaling constant η controls the relative strength of loss guidance. By using annealed Langevin dynamics (Song and Ermon, 2019), it is possible to use the predicted score function together with the loss term to sample from an approximation to $\hat{q}(\mathbf{z}_0|\mathbf{y})$. While this provides a clear interpretation for the effect of loss guidance, the cost of annealed Langevin dynamics can be fairly large. Instead, we solve the probability flow ODE using the score function

$$\hat{\mathbf{s}}_{\theta}(\mathbf{z}_t, t) := \mathbf{s}_{\theta}(\mathbf{z}_t, t) - \eta \nabla_{\mathbf{z}_t} \ell_{\mathbf{y}}(\mathbf{z}_t). \quad (14)$$

This no longer corresponds to sampling from an approximation to $\hat{q}(\mathbf{z}_0|\mathbf{y})$ (see (Song et al., 2023)), however, so long as the latents \mathbf{z}_t are not too out-of-distribution with respect to the marginals $q(\mathbf{z}_t|\mathbf{y})$, then, much like CFG (Ho and Salimans, 2021), this process influences the trajectory to favor samples from $p_{\theta}(\mathbf{z}_0|\mathbf{y})$ for which the loss term is small.

For layout control, given a list of target tokens $S \subset \{1, 2, \dots, k\}$, we choose the simple loss function

$$\ell_{\mathbf{y}}(\mathbf{z}_t) = \sum_{j \in S} g_{\text{IB}}(\bar{\mathbf{m}}_j \odot (A_t)_j) - g_{\text{OB}}(\mathbf{m}_j \odot (A_t)_j), \quad (15)$$

where \mathbf{m}_j is a mask whose value is 1 over the region where token \mathbf{y}_j should appear, and 0 otherwise, and $\bar{\mathbf{m}}_j = 1 - \mathbf{m}_j$. Intuitively, this simple loss encourages sampling latents whose attention maps for each target token take their largest values within the masked regions.

The specific choices of g_{IB} and g_{OB} heavily influence the behaviour of loss-guidance. In BoxDiff, Xie et al. (2023) use sums over the $P \ll n$ most attended-to pixels in the masked attention maps. This seems to be an essential step for maintaining good image quality at very high levels of loss guidance. Since we will use much lower levels of loss guidance, we find that choosing $g_{\text{IB}} = g_{\text{OB}} = \text{sum}(\cdot)$ works well to contain the attentions within the regions defined by m .

In practice, diffusion models are trained to predict the normalized noise $\epsilon \sim \mathcal{N}(\mathbf{0}, \mathbf{I})$ in \mathbf{z}_t . Revisiting Eq. (7), we observe that we can define the corresponding modified noise prediction by scaling the loss-guidance term appropriately (Dhariwal and Nichol, 2021):

$$\hat{\epsilon}_{\theta}(\mathbf{z}_t, t) := \epsilon_{\theta}(\mathbf{z}_t, t) + \eta \sigma_t \nabla_{\mathbf{z}_t} \ell_{\mathbf{y}}(\mathbf{z}_t). \quad (16)$$

4.3 iLGD

One weakness of attention injection is that, by directly modifying the attention maps, we disrupt the agreement between the predicted score function $\mathbf{s}_{\theta}(\mathbf{z}_t, t)$ and the true conditional score



Figure 3: Images generated with the prompt “a ball on the grass,” using the bounding boxes shown in the first column. Each row corresponds to a different method. The bounding boxes in the first column are used for injection and iLGD. The attention maps in the second column are averages over the 8×8 resolution attention maps at $t = 0$ over 100 random seeds. Each of the 8 columns of images in this figure corresponds to one of these 100 seeds.

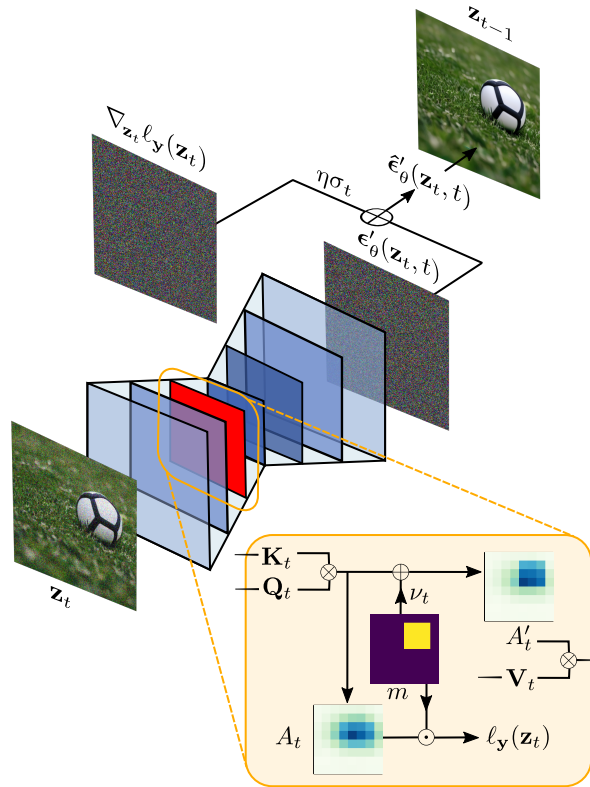


Figure 4: A graphical depiction of injection loss guidance (iLGD).

$\nabla_{\mathbf{z}_t} \log q(\mathbf{z}_t|\mathbf{y})$. The discrepancy between the actual and predicted score functions becomes especially pronounced at smaller noise levels, where fine details in the cross attention maps are destroyed by the injection process. This results in a cartoon-like appearance in the final sampled images, as seen in Figure 17 of (Balaji et al., 2023) and in the bottom row of Figure 2. The sensitivity of the cross-attention maps at low noise levels makes it difficult to use injection to precisely control the final layout, without negatively influencing image quality. One big advantage of attention injection, however, is that at high noise levels it is possible to strongly influence the cross-attention maps while still producing latents that are in-distribution. Interestingly, even the cartoon-like images resulting from excessive attention injection at low noise levels are not actually out-of-distribution, but are only in an unwanted style.

A weakness of loss-guidance is that the ad-hoc choice of the loss function may not compete well with the predicted score $\mathbf{s}_\theta(\mathbf{z}_t, t)$. In each denoising step, the latent \mathbf{z}_{t-1} must fall in a high probability region of $q(\mathbf{z}_{t-1}|\mathbf{z}_t)$, otherwise the predicted latent \mathbf{z}_{t-1} will be out-of-distribution, which results in degraded image quality in the final sampled latent \mathbf{z}_0 . This means that the guidance term’s influence in Eq. (12) should be small enough to avoid moving the latents into low probability regions. On the other hand, small loss guidance strengths may exert too little influence on the sampling trajectory. In this case, the model produces in-distribution samples, but ones which do not fully agree with the desired layout. This tradeoff is illustrated in the first row of Figure 2. One advantage of loss-guidance is that, even at low strengths, it is able to exert some influence over sampling trajectories without biasing the style of the images.

We take the point of view that injection is better suited as a course control over the predicted latents, and cannot fully replace loss guidance. Instead, we propose using injection together with loss guidance in a complimentary fashion, in such a way that they compensate for each other’s weaknesses. We call this approach to layout control injection loss guidance (iLGD). Instead of delegating the layout generation task entirely to loss guidance, we rely on injection to first bias the latent, as illustrated in the second row of Figure 3. The first row of this figure shows that, when using Stable Diffusion alone, the ball appears in random locations near the center of the image, while the second row shows that injection encourages it to appear more frequently inside of the bounding box, towards the top right. When we also perform loss guidance, the third row of the figure shows that the averaged attention map is significantly more concentrated inside of the bounding box. Since the original score function is modified additively, the amount of loss guidance can be made sufficiently small so that the latents stay in-distribution, while still being large enough to influence the sampling trajectory. This is true even at small noise levels, when fine details are present in the images.

We also observe that, when using both injection and loss guidance, the details of the objects better reflect the context of the scene due to higher levels of attention on those objects. In the third row, many of the balls appear in the style of a soccer ball, which is likely the most common type of ball to appear together with grass.

We outline our algorithm in Algorithm 1 and depict it visually in Figure 4. We perform attention injection from timestep T to t_{inject} in order to obtain the modified predicted noise $\epsilon'_\theta(\mathbf{z}_t, t)$. In each timestep, we further refine this latent by performing loss-guidance simultaneously, from timestep T to t_{loss} . In practice, we find it useful to perform loss-guidance for several more steps after we stop injection, $t_{\text{loss}} > t_{\text{inject}}$.

ALGORITHM 1: Pseudocode for iLGD

Input: A prompt \mathbf{y} ; a list of target tokens $S \subset \{1, 2, \dots, k\}$; a collection of bounding boxes, one for each token in S ; an injection strength ν' ; a loss guidance strength η .
Output: The generated image $\mathbf{x}_0 = \mathcal{D}(\mathbf{z}_0)$.
Construct the mask $m = \{\mathbf{m}_1, \mathbf{m}_2, \dots, \mathbf{m}_k\}$ from the bounding boxes;
Initialize $\mathbf{z}_T \sim \mathcal{N}(\mathbf{0}, \mathbf{I})$;
for $t = T, \dots, 1$ **do**
 $\epsilon'_\theta(\mathbf{z}_t, t) = \begin{cases} \epsilon_\theta(\mathbf{z}_t, t, A_t \xrightarrow{\nu', m} A'_t) & \text{if } t > t_{\text{inject}}, \\ \epsilon_\theta(\mathbf{z}_t, t) & \text{otherwise} \end{cases}$;
 $\ell_{\mathbf{y}}(\mathbf{z}_t) = \begin{cases} \sum_{j \in S} g_{\text{IB}}(\bar{\mathbf{m}}_j \odot (A_t)_j) - g_{\text{OB}}(\mathbf{m}_j \odot (A_t)_j) & \text{if } t > t_{\text{loss}}, \\ 0 & \text{otherwise} \end{cases}$;
 $\hat{\epsilon}'_\theta(\mathbf{z}_t, t) = \epsilon'_\theta(\mathbf{z}_t, t) + \eta \sigma_t \nabla_{\mathbf{z}_t} \ell_{\mathbf{y}}(\mathbf{z}_t)$;
 Compute \mathbf{z}_{t-1} from \mathbf{z}_t using $\hat{\epsilon}'_\theta(\mathbf{z}_t, t)$;
end

5 Experiments

5.1 Experimental Setup

Datasets We follow Xie et al. (2023) and evaluate performance on a dataset consisting of 200 prompt and bounding box pairs, spanning 20 different prompts and 27 object categories. Each prompt reflects either of the following prompt structures: “a { } ...,” or “a { } and a { } ...”

Evaluation Metrics We employ a variety of metrics to measure performance along various aspects. First, we use the T2I-Sim metric (Xie et al., 2023) to measure text-to-image similarity between prompts and their corresponding generated images. This metric measures the cosine similarity between text and images in CLIP feature space (Radford et al., 2021) to evaluate how well the generated images reflect the semantics of the prompt.

We also use CLIP-IQA (Wang et al., 2023) to assess the quality of the generated images. Given a pair of descriptors $\{\mathbf{y}_1, \mathbf{y}_2\}$ which are opposite in meaning (e.g., high quality, low quality), CLIP-IQA compares the CLIP features of these prompts with the CLIP features of the generated image. The final score reflects how well \mathbf{y}_1 , as opposed to \mathbf{y}_2 , describes the image. We evaluate the overall quality of images using the pair {high quality, low quality}, blurriness using {clear, blurry}, and naturalness using {natural, synthetic}.

To evaluate each method’s faithfulness to the prescribed bounding box, we use YOLOv4 (Bochkovskiy et al., 2020) to compare the predicted bounding boxes over the set of generated images to the ground truth bounding boxes, and report the average precision at IOU = 0.5.

Finally, we report the average contrast and saturation of generated images. We observe that guidance-based methods often lead to high contrast and high saturation, particularly when the guidance strength is high.

More details about these evaluation metrics can be found in Appendix C.

5.2 Implementation Details

We implemented our method on the official Stable Diffusion v1.4 model (Rombach et al., 2022) from HuggingFace. All images are generated using 50 denoising steps and a classifier-free guid-

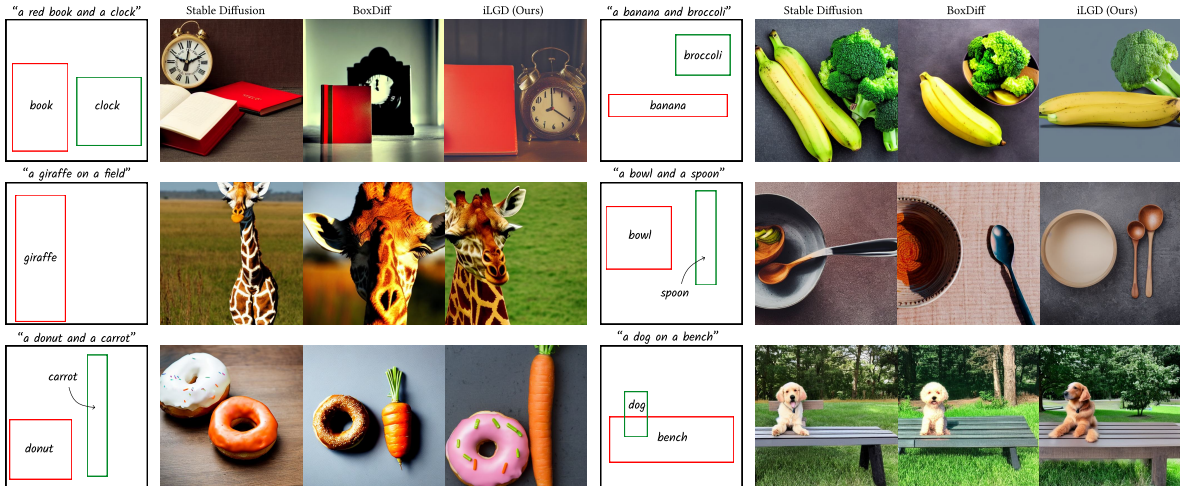


Figure 5: A comparison of iLGD against BoxDiff and Stable Diffusion. The random seed is kept the same across each set of images.

ance scale of 7.5, unless otherwise noted. We use the noise scheduler `LMSSDiscreteScheduler` (Karras et al., 2022) provided by HuggingFace. Experiments were conducted on an NVIDIA TESLA V100 GPU.

We perform attention injection over all attention maps. When performing injection, we resize the mask m to the appropriate resolution, depending on which layer of the UNet the attention maps are taken from. For loss guidance, we again use all of the model’s attention maps, but resize them 16×16 resolution, and compute the mean of each map over all pixels. We apply the softmax function over these means to obtain a weight vector \mathbf{w} , where each entry w_j is the scalar weight associated with the j -th resized attention map. Finally, we obtain the attention map A_t by taking a weighted average over all resized attention maps at time t , using the appropriate weight w_j for each map.

When attempting to control the layout of a generated image, we find that skipping the first step, so that it remains a standard denoising step, leads to better results. We do this for all experiments conducted in this paper which use either injection or loss guidance or both. We use $\eta = 0.48$, $\nu' = 0.75$, $t_{\text{loss}} = 25$, and $t_{\text{inject}} = 10$, unless otherwise noted.

In our comparisons with BoxDiff, we maintain the default parameters the authors provide in their implementation. We start with $\alpha_T = 20$, which decays linearly to $\alpha_0 = 10$, and perform guidance for 25 denoising steps out of a total of 50 steps.

5.3 Comparisons

We present a comparison between our proposed method (iLGD), BoxDiff (Xie et al., 2023), and Stable Diffusion (Rombach et al., 2022) in Figure 5. Qualitatively, we observe that BoxDiff produces images with much higher contrast and saturation. For instance, for the prompt “a donut and a carrot,” both objects in BoxDiff’s image appear unnaturally bright or dark in certain regions. Similarly, Figure 2 indicates that BoxDiff produces images with very high contrast, e.g., the light shade of the bread and the dark shade of the bottle, and saturation, e.g., the red of the tomatoes, when using high loss guidance strengths to produce the desired layout. High contrast and saturation are even visible in some images when just Stable Diffusion

Table 1: Comparison of the average contrast and saturation over 200 images for BoxDiff, Stable Diffusion (SD), and iLGD.

	Average Contrast	Average Saturation
Ours (iLGD)	47.53	105.81
SD @ CFG 0.0	52.96	84.49
SD @ CFG 7.5	58.53	110.14
SD @ CFG 12.5	65.87	123.32
BoxDiff	65.68	115.67
SD + Injection	46.07	105.63
SD + Loss Guidance	58.51	102.62

Table 2: Comparison of various quality metrics for BoxDiff, Stable Diffusion (SD), and iLGD, averaged over 200 images.

Method	T2I-Sim (\uparrow)	CLIP-IQA (\uparrow)			AP@0.5 (\uparrow)
		Quality	Natural	Clear	
SD	0.303	0.928	0.705	0.736	–
BoxDiff	0.305	0.922	0.613	0.6945	0.192
SD + Injection	0.305	0.958	0.647	0.808	0.136
SD + Loss Guidance	0.302	0.932	0.684	0.737	0.055
Ours (iLGD)	0.309	0.961	0.654	0.817	0.202

is used, e.g., in the prompts “a balloon and a cake and a frame...” and “a suitcase and a handbag” in Figure 6.

These observations are reflected quantitatively in Table 1, which reports the average contrast and saturation across all generated images. The same high-contrast and high-saturation phenomenon observed in BoxDiff is seen to occur in Stable Diffusion when increasing the classifier-free guidance (CFG) scale. Both loss guidance and CFG appear to move the predicted latent into similar low-probability regions if the strength is too large, which may nonetheless be necessary to obtain either the appropriate layout or the appropriate agreement with the semantics of the text prompt. Attention injection does not appear to have this biasing effect, and the contrast and saturation for iLGD are similar to those of attention injection.

We note that both attention injection and iLGD produce images of lower contrast than even Stable Diffusion without classifier-free guidance, although visual inspection suggests that this does not manifest as any obvious abnormality in the images. We hypothesize that injection favours scenes that naturally contain lower contrast. When the objects appearing in the images receive high levels of attention as a result of injection, they tend to be clear, in-focus, and easily discernible, and do not have either very bright reflections or very dark shadows.

Biasing the latents using injection also clearly helps to preserve image quality and achieve stronger layout control, particularly for layouts which are difficult for the model to generate. For the prompt “a red book and a clock,” BoxDiff struggles to move the clock into the correct position, instead generating it as a lower quality, shadow-like figure. Using iLGD, the clock maintains its fine details, e.g., the numbering on the face, as well as its texture. For the prompt “a bowl and a spoon,” the image produced by iLGD is more faithful to the bounding boxes, whereas BoxDiff has difficulty reorienting the scene. The bowl remains in the same position

as it was with Stable Diffusion alone, and it becomes difficult to distinguish the spoon from its shadow as dark colours are exaggerated.

In Table 2, we report various metrics related to image quality (CLIP-IQA), bounding box precision (YOLOv4), and text-to-image similarity (T2I-Sim). While both BoxDiff and iLGD achieve similar T2I-Sim and AP@0.5 scores, the latter achieves better performance on all CLIP-IQA metrics. This indicates that iLGD is able to achieve superior image quality without sacrificing layout control, qualifying it as a meaningful improvement over BoxDiff.

We provide additional comparisons in Appendix B.

5.4 Ablation Studies

To understand the effectiveness of iLGD, we compare it against injection alone. Figure 6 presents a visual comparison between the two methods. We observe that, while injection typically does generate an object in each bounding box, the object itself may be incorrect. To illustrate, for the prompt “a balloon, a cake, and a frame, . . .,” using injection leads to a frame appearing where the cake should be; for “a donut and a carrot,” it generates a hand where the donut should be; for “a suitcase and a handbag,” a second suitcase is generated instead of a handbag; and for “a cat sitting outside,” something akin to a tree stump appears instead of a cat. In the example for “a castle in the middle of a marsh,” the castle does not fill up the bounding box, and for “a cat with a tie” the resulting image has the correct layout, but begins to appear like a cartoon cutout. When loss guidance is added using iLGD, all of these images appear correctly. These observations are reflected in Table 2, where iLGD achieves a noticeably higher AP@50 score compared to injection.

We note that the results in Figure 6 provide some additional evidence that injection is able to successfully bias the image according to the desired layout. For instance, revisiting the example of the prompt “a cat sitting outside,” injection causes a tree stump to appear in the region where the attention was enhanced. When loss guidance is also applied in each step, this stump is instead denoised into a cat. In this case, a small amount of loss guidance suffices to generate the appropriate layout, as it is augmented by the biasing effect of injection.

6 Conclusions

In this work, we introduce a framework which combines both attention injection and loss guidance to produce samples conforming to a desired layout. We show, both qualitatively and quantitatively, that our proposed method can produce such samples with fewer visual artifacts compared to training-free methods using loss guidance alone. Our method uses only existing components of the diffusion model, avoiding any additional model complexity. One of the method’s limitations is that it remains somewhat sensitive to the initial random seed.

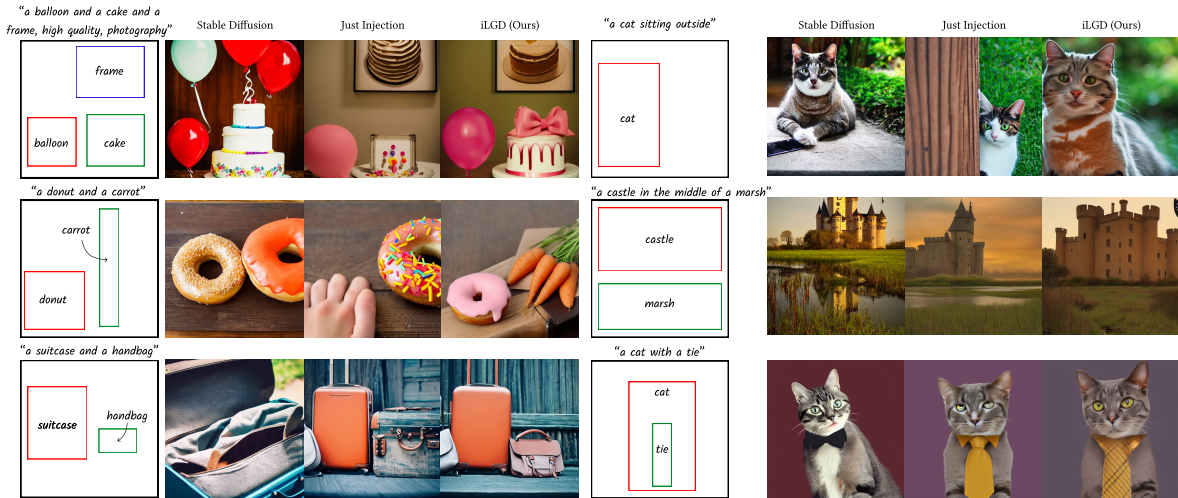


Figure 6: Images generated using either just injection or iLGD. The random seed is kept the same across each set of images. For the prompt “a castle in the middle of a marsh,” we use $\nu' = 0.6$ for injection and use $\eta = 0.48$ when we additionally introduce loss guidance in iLGD.

References

- Yogesh Balaji, Seungjun Nah, Xun Huang, Arash Vahdat, Jiaming Song, Qinsheng Zhang, Karsten Kreis, Miika Aittala, Timo Aila, Samuli Laine, Bryan Catanzaro, Tero Karras, and Ming-Yu Liu. 2023. eDiff-I: Text-to-Image Diffusion Models with an Ensemble of Expert Denoisers. *arXiv preprint arXiv:2211.01324* (2023).
- Arpit Bansal, Hong-Min Chu, Avi Schwarzschild, Soumyadip Sengupta, Micah Goldblum, Jonas Geiping, and Tom Goldstein. 2024. Universal Guidance for Diffusion Models. In *ICLR*.
- Omer Bar-Tal, Lior Yariv, Yaron Lipman, and Tali Dekel. 2023. Multidiffusion: Fusing Diffusion Paths for Controlled Image Generation. 202 (2023), 1737–1752.
- Alexey Bochkovskiy, Chien-Yao Wang, and Hong-Yuan Mark Liao. 2020. YOLOv4: Optimal Speed and Accuracy of Object Detection.
- Minghao Chen, Iro Laina, and Andrea Vedaldi. 2024. Training-Free Layout Control with Cross-Attention Guidance. In *IEEE Wint. Conf. Appl.* 5343–5353.
- Jiaxin Cheng, Xiao Liang, Xingjian Shi, Tong He, Tianjun Xiao, and Mu Li. 2023. Layoutdiffuse: Adapting foundational diffusion models for layout-to-image generation. *arXiv preprint arXiv:2302.08908* (2023).
- Guillaume Couairon, Marlène Careil, Matthieu Cord, Stéphane Lathuilière, and Jakob Verbeek. 2023. Zero-shot Spatial Layout Conditioning for Text-to-Image Diffusion Models. In *ICCV*. 2174–2183.
- Prafulla Dhariwal and Alexander Nichol. 2021. Diffusion Models Beat GANs on Image Synthesis. *NeurIPS* 34 (2021), 8780–8794.

- Bradley Efron. 2011. Tweedie’s Formula and Selection Bias. *J. Am. Stat. Assoc.* 106, 496 (2011), 1602–1614.
- Dave Epstein, Allan Jabri, Ben Poole, Alexei Efros, and Aleksander Holynski. 2023. Diffusion Self-Guidance for Controllable Image Generation. In *NeurIPS*, Vol. 36. 16222–16239.
- Mathieu Germain, Karol Gregor, Iain Murray, and Hugo Larochelle. 2015. Made: Masked Autoencoder for Distribution Estimation. In *ICML*, Vol. 37.
- Ian Goodfellow, Jean Pouget-Abadie, Mehdi Mirza, Bing Xu, David Warde-Farley, Sherjil Ozair, Aaron Courville, and Yoshua Bengio. 2014. Generative Adversarial Nets. In *NeurIPS*, Vol. 27.
- Amir Hertz, Ron Mokady, Jay Tenenbaum, Kfir Aberman, Yael Pritch, and Daniel Cohen-or. 2023. Prompt-to-Prompt Image Editing with Cross-Attention Control. In *ICLR*.
- Jonathan Ho, Ajay Jain, and Pieter Abbeel. 2020. Denoising Diffusion Probabilistic Models. *NeurIPS* 33, 6840–6851.
- Jonathan Ho and Tim Salimans. 2021. Classifier-Free Diffusion Guidance. In *NeurIPS (Workshop: Deep Generative Models and Downstream Applications)*.
- Tero Karras, Miika Aittala, Timo Aila, and Samuli Laine. 2022. Elucidating the Design Space of Diffusion-Based Generative Models. In *NeurIPS*, Vol. 35.
- Diederik P. Kingma and Max Welling. 2014. Auto-Encoding Variational Bayes. In *ICLR*.
- Zejian Li, Jingyu Wu, Immanuel Koh, Yongchuan Tang, and Lingyun Sun. 2021. Image Synthesis From Layout with Locality-Aware Mask Adaption. In *ICCV*. 13819–13828.
- Cheng Lu, Yuhao Zhou, Fan Bao, Jianfei Chen, Chongxuan Li, and Jun Zhu. 2022. DPM-Solver: A Fast ODE Solver for Diffusion Probabilistic Model Sampling in Around 10 Steps. In *NeurIPS*, Vol. 35.
- Chenlin Meng, Yutong He, Yang Song, Jiaming Song, Jiajun Wu, Jun-Yan Zhu, and Stefano Ermon. 2022. SDEdit: Guided Image Synthesis and Editing with Stochastic Differential Equations. In *ICLR*.
- Aäron van den Oord, Nal Kalchbrenner, Oriol Vinyals, Lasse Espeholt, Alex Graves, and Koray Kavukcuoglu. 2016. Conditional Image Generation with PixelCNN Decoders. In *NeurIPS*, Vol. 29.
- Rafael Padilla, Sergio L Netto, and Eduardo AB Da Silva. 2020. A Survey on Performance Metrics for Object-Detection Algorithms. In *Int. Conf. Syst. Signal.* IEEE, 237–242.
- Alec Radford, Jong Wook Kim, Chris Hallacy, Aditya Ramesh, Gabriel Goh, Sandhini Agarwal, Girish Sastry, Amanda Askell, Pamela Mishkin, Jack Clark, et al. 2021. Learning transferable visual models from natural language supervision. In *ICML*. PMLR, 8748–8763.
- Aditya Ramesh, Prafulla Dhariwal, Alex Nichol, Casey Chu, and Mark Chen. 2022. Hierarchical Text-Conditional Image Generation with Clip Latents. *arXiv preprint arXiv:2204.06125* (2022).

- Danilo Rezende and Shakir Mohamed. 2015. Variational Inference with Normalizing Flows. In *ICML*, Vol. 37. PMLR, 1530–1538.
- Robin Rombach, Andreas Blattmann, Dominik Lorenz, Patrick Esser, and Björn Ommer. 2022. High-resolution Image Synthesis with Latent Diffusion Models. In *CVPR*. 10684–10695.
- Olaf Ronneberger, Philipp Fischer, and Thomas Brox. 2015. U-Net: Convolutional Networks for Biomedical Image Segmentation. In *MICCAI*. 234–241.
- Chitwan Saharia, William Chan, Saurabh Saxena, Lala Li, Jay Whang, Emily L Denton, Kamyar Ghasemipour, Raphael Gontijo Lopes, Burcu Karagol Ayan, Tim Salimans, et al. 2022. Photorealistic Text-to-Image Diffusion Models with Deep Language Understanding. *NeurIPS* 35 (2022), 36479–36494.
- Tim Salimans, Andrej Karpathy, Xi Chen, and Diederik P. Kingma. 2017. PixelCNN++: Improving the PixelCNN with Discretized Logistic Mixture Likelihood and Other Modifications. In *ICLR*. Poster.
- Jaskirat Singh, Stephen Gould, and Liang Zheng. 2023. High-Fidelity Guided Image Synthesis with Latent Diffusion Models. In *CVPR*. IEEE, 5997–6006.
- Jascha Sohl-Dickstein, Eric Weiss, Niru Maheswaranathan, and Surya Ganguli. 2015. Deep Unsupervised Learning Using Nonequilibrium Thermodynamics. In *ICML*, Vol. 37. PMLR, 2256–2265.
- Jiaming Song, Qinsheng Zhang, Hongxu Yin, Morteza Mardani, Ming-Yu Liu, Jan Kautz, Yongxin Chen, and Arash Vahdat. 2023. Loss-Guided Diffusion Models for Plug-and-Play Controllable Generation. In *ICML*, Vol. 202. PMLR, 32483–32498.
- Yang Song and Stefano Ermon. 2019. Generative Modeling by Estimating Gradients of the Data Distribution. *NeurIPS* 32 (2019).
- Yang Song, Jascha Sohl-Dickstein, Diederik P Kingma, Abhishek Kumar, Stefano Ermon, and Ben Poole. 2021. Score-Based Generative Modeling through Stochastic Differential Equations. In *ICLR*.
- Aäron Van Den Oord, Nal Kalchbrenner, and Koray Kavukcuoglu. 2016. Pixel Recurrent Neural Networks. In *ICML*, Vol. 48. 1747–1756.
- Ashish Vaswani, Noam Shazeer, Niki Parmar, Jakob Uszkoreit, Llion Jones, Aidan N Gomez, Lukasz Kaiser, and Illia Polosukhin. 2017. Attention is All You Need. *NeurIPS* 30, 5998–6008.
- Pascal Vincent. 2011. A Connection between Score Matching and Denoising Autoencoders. *Neural Comput.* 23, 7 (2011), 1661–1674.
- Andrey Voynov, Kfir Aberman, and Daniel Cohen-Or. 2023. Sketch-Guided Text-to-Image Diffusion Models. In *SIGGRAPH*. 1–11.
- Jianyi Wang, Kelvin CK Chan, and Chen Change Loy. 2023. Exploring CLIP for Assessing the Look and Feel of Images. In *AAAI*, Vol. 37. 2555–2563.

Jinheng Xie, Yuexiang Li, Yawen Huang, Haozhe Liu, Wentian Zhang, Yefeng Zheng, and Mike Zheng Shou. 2023. Boxdiff: Text-to-Image Synthesis with Training-Free Box-Constrained Diffusion. In *ICCV*. 7452–7461.

Lvmin Zhang, Anyi Rao, and Maneesh Agrawala. 2023. Adding Conditional Control to Text-to-Image Diffusion Models. In *ICCV*. 3836–3847.

Guangcong Zheng, Xianpan Zhou, Xuewei Li, Zhongang Qi, Ying Shan, and Xi Li. 2023. Layoutdiffusion: Controllable Diffusion Model for Layout-to-Image Generation. In *CVPR*. 22490–22499.

A Diffusion Models

A.1 Denoising Diffusion Probabilistic Models

In denoising diffusion probabilistic models (DDPM) (Ho et al., 2020), the forward process is characterized by the Markov chain $q(\mathbf{x}_t|\mathbf{x}_{t-1}) \sim \mathcal{N}(\mathbf{x}_t; \sqrt{1 - \beta_t}\mathbf{x}_{t-1}, \beta_t\mathbf{I})$, for some noise schedule β_t . In this case, $q(\mathbf{x}_t|\mathbf{x}_0) \sim \mathcal{N}(\mathbf{x}_t; \sqrt{\bar{\alpha}_t}\mathbf{x}_0, (1 - \bar{\alpha}_t)\mathbf{I})$, where $\bar{\alpha}_t = \prod_{s=1}^t \alpha_s$ and $\alpha_t = 1 - \beta_t$. The reverse process is typically modeled by a learned Markov chain $p_\theta(\mathbf{x}_{t-1}|\mathbf{x}_t) \sim \mathcal{N}(\mathbf{x}_{t-1}; \mu_\theta(\mathbf{x}_t, t), \sigma_t^2\mathbf{I})$, where $\sigma_t^2 = \beta_t$.

It is not efficient to optimize the log-likelihood $\mathbb{E}[-\log p_\theta(x_0)]$ directly, since computing $p_\theta(\mathbf{x}_0)$ requires marginalizing over $\mathbf{x}_{1:T}$. Instead, one can use importance sampling to write

$$p_\theta(\mathbf{x}_0) = \mathbb{E}_{q(\mathbf{x}_{1:T}|\mathbf{x}_0)} \left[\frac{p_\theta(\mathbf{x}_{0:T})}{q(\mathbf{x}_{1:T}|\mathbf{x}_0)} \right]. \quad (17)$$

Then, by Jensen’s inequality,

$$-\log p_\theta(\mathbf{x}_0) \leq \mathbb{E}_{q(\mathbf{x}_{1:T}|\mathbf{x}_0)} \left[-\log \frac{p_\theta(\mathbf{x}_{0:T})}{q(\mathbf{x}_{1:T}|\mathbf{x}_0)} \right]. \quad (18)$$

The right hand side is the usual evidence lower bound (ELBO), which is minimized instead. In (Ho et al., 2020), the authors show that minimizing the ELBO is equivalent to minimizing

$$\mathbb{E}_t[\lambda(t)\mathbb{E}_{q(\mathbf{x}_0), \epsilon}[\|\epsilon_\theta(\mathbf{x}_t, t) - \epsilon\|_2^2]], \quad (19)$$

for some $\lambda(t)$, where $\epsilon \sim \mathcal{N}(\mathbf{0}, \mathbf{I})$, $\mathbf{x}_t(\mathbf{x}_0, \epsilon) = \sqrt{\bar{\alpha}_t}\mathbf{x}_0 + \sqrt{1 - \bar{\alpha}_t}\epsilon$, and

$$\mu_\theta(\mathbf{x}_t, t) = \frac{1}{\sqrt{\bar{\alpha}_t}} \left(\mathbf{x}_t - \frac{\beta_t}{\sqrt{1 - \bar{\alpha}_t}} \epsilon_\theta(\mathbf{x}_t, t) \right). \quad (20)$$

A.2 Score Matching

Since $q(x_t|x_0)$ is a normal distribution, we know that

$$\nabla_{\mathbf{x}_t} \log q(\mathbf{x}_t|\mathbf{x}_0) = -\frac{\epsilon}{\sqrt{1 - \bar{\alpha}_t}}. \quad (21)$$

Thus, minimizing (19) is equivalent to minimizing

$$\mathbb{E}_t[\lambda(t)\mathbb{E}_{q(\mathbf{x}_0)}\mathbb{E}_{q(\mathbf{x}_t|\mathbf{x}_0)}[\|\mathbf{s}_\theta(\mathbf{x}_t, t) - \nabla_{\mathbf{x}_t} \log q(\mathbf{x}_t|\mathbf{x}_0)\|_2^2]], \quad (22)$$

for some $\lambda(t)$, where

$$\mathbf{s}_\theta(\mathbf{x}_t, t) := -\frac{\epsilon_\theta(\mathbf{x}_t, t)}{\sqrt{1 - \bar{\alpha}_t}}. \quad (23)$$

It is known that this loss is minimized when $\mathbf{s}_\theta(\mathbf{x}_t, t) = \nabla_{\mathbf{x}_t} \log q(\mathbf{x}_t)$ (Vincent, 2011), so given enough parameters, $\mathbf{s}_\theta(\mathbf{x}_t, t)$ will converge to $\nabla_{\mathbf{x}_t} \log q(\mathbf{x}_t)$ almost everywhere. With this, the mean $\mu_\theta(\mathbf{x}_t, t)$ of the reverse process can be understood as

$$\mu_\theta(\mathbf{x}_t, t) = \sqrt{\bar{\alpha}_{t-1}} D_\theta(\mathbf{x}_t, t) \approx \mathbb{E}_q[\sqrt{\bar{\alpha}_{t-1}} \mathbf{x}_0 | \mathbf{x}_t], \quad (24)$$

where

$$D_\theta(\mathbf{x}_t, t) := \frac{1}{\sqrt{\bar{\alpha}_t}}(\mathbf{x}_t + \beta_t \mathbf{s}_\theta(\mathbf{x}_t, t)) \quad (25)$$

is an approximation to Tweedie’s formula

$$\frac{1}{\sqrt{\bar{\alpha}_t}}(\mathbf{x}_t + \beta_t \nabla_{\mathbf{x}_t} \log q(\mathbf{x}_t)) = \frac{1}{\sqrt{\bar{\alpha}_t}} \mathbb{E}_q[\sqrt{\bar{\alpha}_t} \mathbf{x}_0 | \mathbf{x}_t] = \mathbb{E}_q[\mathbf{x}_0 | \mathbf{x}_t] \quad (26)$$

(Efron, 2011). Given an approximation to the score function, it is possible to sample from $p_\theta(\mathbf{x}_0)$ using annealed Langevin dynamics (Song and Ermon, 2019).

A.3 Stochastic Differential Equations

Song et al. (2021) showed that the forward process of DDPM can be viewed as a discretization of the stochastic differential equation (SDE)

$$d\mathbf{x} = -\frac{1}{2}\beta(t)\mathbf{x} dt + \sqrt{\beta(t)} d\mathbf{w}, \quad (27)$$

where \mathbf{w} denotes the Wiener process. There, the authors point out that any SDE of the form $d\mathbf{x} = \mathbf{f}(\mathbf{x}, t) + g(t)d\mathbf{w}$, where $\mathbf{x}_0 \sim p_0(\mathbf{x}_0)$ can be reversed by the SDE $d\mathbf{x} = (\mathbf{f}(\mathbf{x}, t) - g(t)^2 \nabla_{\mathbf{x}} \log p_t(\mathbf{x})) dt + g(t) d\bar{\mathbf{w}}$, where $\bar{\mathbf{w}}$ is the standard Wiener process in the reverse time direction, and where $\mathbf{x}_T \sim p_T(\mathbf{x}_T)$. Furthermore, each SDE admits a family of related SDEs that share the same marginal distributions $p_t(\mathbf{x}_t)$. One of these SDEs is purely deterministic, and is known as the probability flow ordinary differential equation (ODE).

If the score function $\mathbf{s}_\theta(\mathbf{x}_t, t)$ is available, then it is possible to sample from $p_\theta(\mathbf{x}_0)$ by solving the probability flow ODE, starting with samples from $p_\theta(\mathbf{x}_T)$. This results in a deterministic mapping from noisy images \mathbf{x}_T to clean images \mathbf{x}_0 . This sampling process can be performed quickly with the aid of ODE solvers (Lu et al., 2022).

B Additional Experiments

We provide two additional sets of comparisons between our proposed method (iLGD), BoxDiff, and Stable Diffusion. In Figure B.1, we compare the three methods using same prompts and bounding boxes as in Figure 5, but using a different random seed for each set of images. In Figure B.1, we compare the methods using an entirely new set of prompts and bounding boxes.

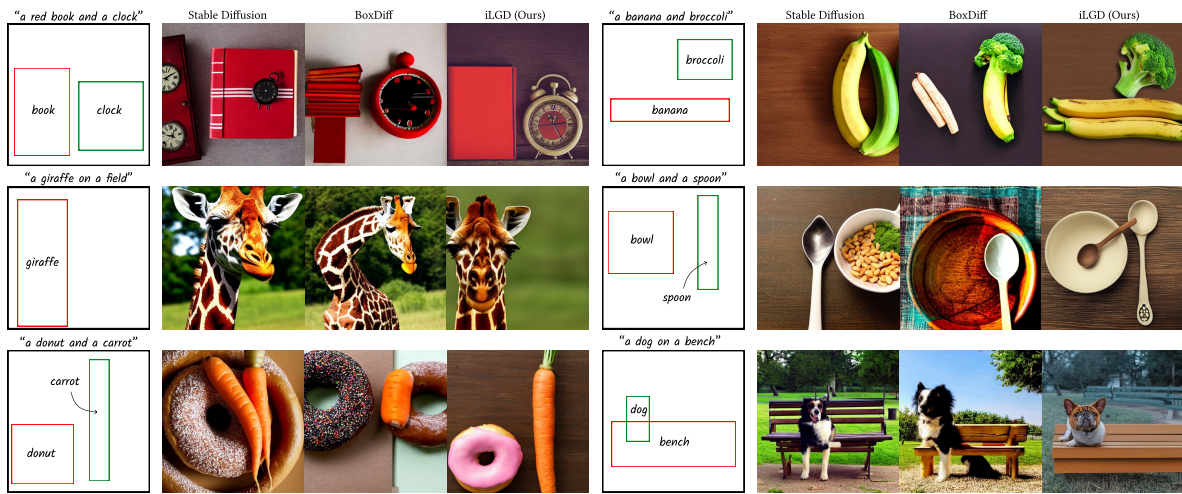


Figure B.1: A comparison of iLGD against BoxDiff and Stable Diffusion, using the same prompts as Figure 5 but different random seeds, with the seed kept the same across each set of images.

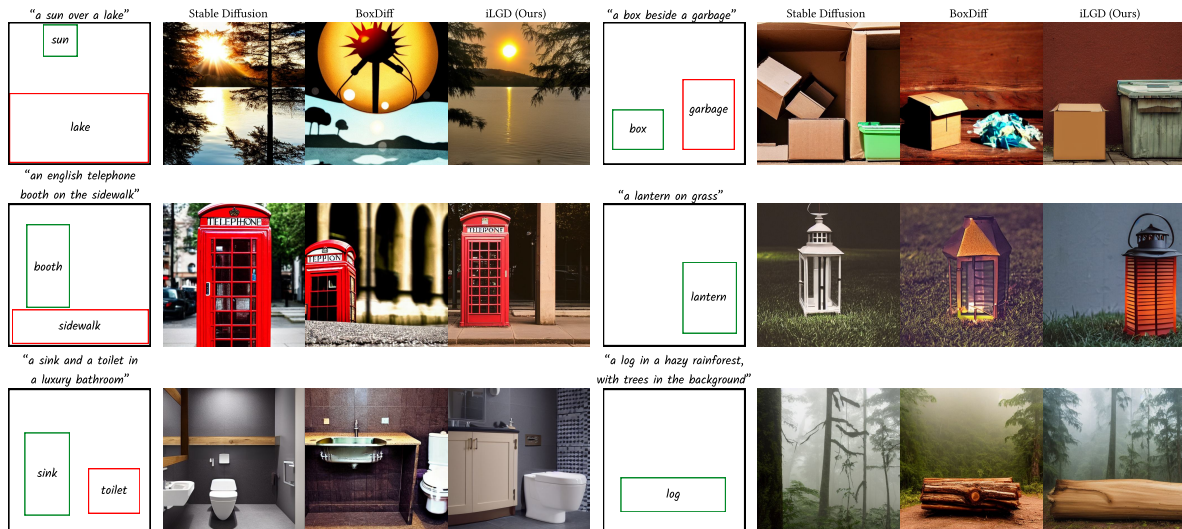


Figure B.2: A comparison of iLGD against BoxDiff and Stable Diffusion, for an entirely new set of prompts. The random seed kept the same across each set of images.

C Detailed Methods

Evaluation with YOLOv4 In this section, we describe in detail how we obtain the AP@50 scores in Table 2. In classical object detection, a model is trained to detect and localize objects of certain classes in an image, typically by predicting a bounding box which fully encloses the object. The accuracy of the model’s predicted bounding box, B_p , is evaluated by comparison to the corresponding ground truth bounding box, B_{gt} . More specifically, we compute the intersection over union (IOU) over the pair of bounding boxes:

$$\text{IOU} = \frac{\text{area}(B_p \cap B_{gt})}{\text{area}(B_p \cup B_{gt})}. \quad (28)$$

The IOU is then compared to a threshold t , such that, if $\text{IOU} \geq t$, then the detection is classified as correct. If not, then the detection is classified as incorrect. In our case, we follow Li et al. (2021) and treat the object detection model as an oracle, where we assume that it provides the bounding boxes of objects in a given image with perfect accuracy, and use the desired layout in place of the ground truth bounding boxes. We generate an image according to our desired layout and apply the object detection model to the generated image to obtain a set of predicted bounding boxes. Finally, to evaluate how similar the layout of the generated image is to the desired layout, we compare each predicted bounding box, B_p , to the corresponding ground truth bounding box, B_{gt} , by computing their IOU. We use a IOU threshold of 0.5.

To calculate the average precision, we first need to compute the number of true positives (TP), false positives (FP), and false negatives (FN). We count a false negative when no detection is made on the image, even though a ground truth object exists, or when the detected class is not among the ground truth classes. We also count a false negative as well as a false positive when the correct detection is made, but $\text{IOU} < 0.5$, and a true positive when $\text{IOU} \geq 0.5$. Using these quantities, we compute the precision P and recall R as:

$$P = \frac{TP}{TP + FP}, \quad (29)$$

$$R = \frac{TP}{TP + FN}. \quad (30)$$

We repeat this for classifier confidence thresholds of 0.15 to 0.95, in steps of 0.05, so that we end up with 17 values for precision and recall, respectively. We then construct a precision-recall curve, and compute the average precision using 11-point interpolation (Padilla et al., 2020):

$$\text{AP}_{11} = \frac{1}{11} \sum_{R \in \{0, 0.1, \dots, 0.9, 1\}} P_{\text{interp}}(R), \quad (31)$$

where

$$P_{\text{interp}}(R) = \max_{\tilde{R} \geq R} P(\tilde{R}). \quad (32)$$

Image Quality Assessment Wang et al. (2023) suggest using the pair {good photo, bad photo} instead of {high quality, low quality} to measure quality, as they find that it corresponds better to human preferences. However, we choose the latter to remain agnostic to the image’s style, as we believe the former carries with it a stylistic bias, due to the word “photo.”

Contrast Calculation We calculate the RMS contrast by using OpenCV’s `.std()` method on a greyscale image.

Saturation Calculation We calculate the saturation by working in HSV space and using OpenCV’s `.mean()` method on the image’s saturation channel.